

Hard X-Ray Properties of Groups of Galaxies as Observed with ASCA

Kazuhiro NAKAZAWA

Institute of Space and Astronautical Science, JAXA, 3-1-1 Yoshino-dai, Sagami-hara, Kanagawa 229-8510

nakazawa@astro.isas.jaxa.jp

Kazuo MAKISHIMA *

Department of Physics, University of Tokyo, 7-3-1 Hongo, Bunkyo-ku, Tokyo 113-0033

and

Yasushi FUKAZAWA

Department of Physical Science, Hiroshima University, 1-3-1 Kagamiyama, Higashi-hiroshima, Hiroshima 739-8526

(Received 2006 September 25; accepted 2006 November 21)

Abstract

X-ray spectra of groups of galaxies, obtained with the GIS instrument onboard ASCA, were investigated for diffuse hard X-rays in excess of the soft thermal emission from their inter-galactic medium (IGM). In total, 18 objects with the IGM temperature of 0.7–1.7 keV were studied, including HCG 62 in particular. Non X-ray backgrounds in the GIS spectra were carefully estimated and subtracted. The IGM emission was represented by up to two temperature thermal models, which was determined in a soft energy band below 2.5 keV mainly by the SIS data. When extrapolated to a higher energy range of 4–8 keV, this thermal model under-predicted the background-subtracted GIS counts in HCG 62 and RGH 80 by $> 2\sigma$ significance, even though the background uncertainties and the IGM modeling errors are carefully accounted. A hard excess could be also present in NGC 1399. The excess was successfully explained by a power-law model with a photon index ~ 2 , or a thermal emission with a temperature exceeding ~ 3 keV. In HCG 62, the 2–10 keV luminosity of the excess hard component was found to be 5.5×10^{41} erg s $^{-1}$ at 2–10 keV, which is ~ 30 percent of the thermal IGM luminosity in 0.7–2.5 keV. Non-thermal and thermal interpretations of this excess components are discussed.

Key words: galaxies: intergalactic medium — galaxies: clusters: general — X-rays: galaxies: clusters

1. Introduction

Clusters of galaxies shows rich evidence for huge energy input within their vast inter-galactic space. Mega-parsec scale radio halos observed in many rich clusters provide direct evidence of GeV electrons accelerated within them (e.g. Feretti, Giovannini 1996). Significant temperature variations in the cluster hot gas, detected by ASCA (e.g. Furusho et al. 2001) as well as Chandra and XMM-Newton (e.g. Markevitch et al. 2003 ; Briel et al. 2004), can be interpreted as relics of energy dissipation associated with cluster mergers. Another striking feature is so called “cavity” in the cluster centers (e.g. Birzan et al. 2004), which is suggestive of an energy input at a level as high as 10^{58-60} erg. These new violent features of clusters of galaxies challenge the classical view of a single phase hot plasma hydrostatically filling the gravitational potential formed by a dark matter halo. The intra-cluster volume, for example, may harbor plasma components much hotter than the virial temperature and/or a significant amount of non-thermal particle population.

The same stroy may apply also to groups of galaxies, the subject of the present paper. They hosts a fair amount of hot gas, called inter-galactic medium (IGM) with a temperature of about 1 keV (see e.g. Mulchaey et al. 1996).

X-ray emission from the IGM is dominated by Fe-L shell lines which appear in the soft X-ray range around 0.6-1.4 keV. Since the emissivity of IGM is very low in energies above 2 keV, we can search this “hard” energy region of the X-ray spectra of groups of galaxies for any additional harder emission component, such as thermal signals from hotter plasmas mixed in the IGM or non-thermal emission from accelerated particles.

The ASCA mission (Tanaka et al. 1994), operated from 1993 to 2000, was equipped with four X-ray mirror optics covering the energy range up to ~ 10 keV. Although their angular resolution was limited, the total effective area of ASCA at 6 keV is larger than that of Chandra. Furthermore, the GIS experiment (Makishima et al. 1996; Ohashi et al. 1996) onboard ASCA is characterized by its very low and stable background, together with a wide field of view ($\sim 45'$ in diameter) and a high quantum efficiency toward ~ 10 keV. Thanks to these properties, the GIS background level normalized to the effective area and sky area, shown in figure 1, has been the lowest among the X-ray detectors with imaging spectroscopic capabilities up to 10 keV. Therefore, data from the GIS is least affected by background uncertainties (both statistical and systematic), which strongly limit the sensitivity to largely ($\gtrsim 5'$) extended emission in the hard X-ray band above ~ 4 keV. The power of the GIS detector is demonstrated, for example, by the detection of non-thermal in-

* Also with RIKEN, Wakou-shi, Saitama 351-0198, Japan

verse Compton emission from the radio lobe of Fonax-A (Kaneda et al. 1995). As a result, the ASCA GIS archive is expected, even today, to provide the best opportunity to search for excess hard X-ray signals from groups of galaxies. Its main drawback, namely the poor sensitivity for exclusion of contaminating point sources, can be compensated for by referring to the public data with higher angular resolution, such as ROSAT and Chandra.

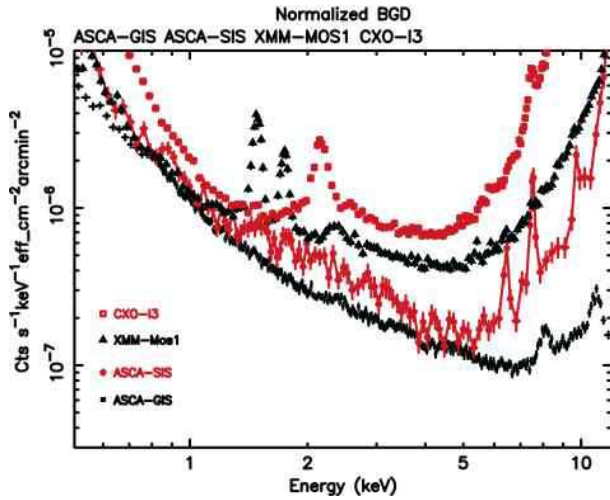


Fig. 1. Background spectra of imaging X-ray detectors per sky area, normalized also to the mirror effective area. Results of the ASCA GIS and the SIS (this work) are compared with those of the Chandra ACIS I 3 and the XMM-Newton EPIC mos 1 (from template background files). Spectra are extracted from a central 15' circular region for the GIS, one full chip for the SIS and ACIS I 3, and a central 8'.5 circular region for EPIC mos. The effective area is for a point source on the nominal aim-point of each detector. The cosmic X-ray background is included.

Based on this idea, Fukazawa et al. (2001) analyzed the ASCA data of a compact galaxy group HCG 62, and discovered evidence for a hard X-ray excess above the thermal IGM emission. Their approach is considered applicable not only to this particular group, but also to almost all near-by low temperature groups. In this paper, we hence study 18 near-by low temperature galaxy groups in the ASCA archive data. In section 2, we present the list of targets with their selection criteria. Section 3 describes the analysis method we employed. Results from the analysis is summarized in section 4. Discussion is presented in section 5, followed by a brief summary in the last section. Throughout the present paper, we assume the Hubble constant to be $H_0 = 75 \text{ km s}^{-1} \text{ Mpc}^{-1}$. All the errors refer to 90 % confidence levels, unless otherwise noted.

2. Target selection

We surveyed all the ASCA archival data for groups of galaxies that are appropriate for our purpose. To separate any additional hard components from the IGM emission within the ASCA band-pass, we need targets with

soft and bright IGM emission. In addition, targets having near-by hard X-ray sources must be avoided, because the wide wing of the point spread function (PSF) of the ASCA mirror degrades the sensitivity. We must avoid even hard sources outside the GIS field of view, because they produce stray lights.

We selected objects which has an IGM temperature lower than 1.7 keV, and the 0.5–10 keV flux higher than $\sim 1 \times 10^{-12} \text{ erg s}^{-1} \text{ cm}^{-2}$. We excluded objects with a luminosity less than $5 \times 10^{41} \text{ erg s}^{-1}$, most of which are isolated elliptical galaxies rather than groups: this is to reduce the hard X-ray contribution from unresolved discrete sources, such as low mass X-ray binaries (LMXBs). We also examined the ROSAT all sky map and other literature for the absence of nearby ($< 2^\circ$) active galactic nuclei (AGN).

The sample thus selected consists of 18 groups, including HCG 62. We list them in table 1 together with their optical properties. Although the sample is far from being complete, it includes variety of objects. There are three Hickson's compact groups, another three (NGC 1132, NGC 1550 and NGC 6521) X-ray selected groups discovered by the ROSAT survey, and 11 relatively loose groups. Their velocity dispersion ranges from $\sigma = 169$ to 474 km s^{-1} .

Table 2 summarizes ASCA observation log of the objects in our sample. The 18 groups are covered by 39 observations in total, of which about one third are offset pointings. We analyzed the GIS data in all observations. In contrast, the SIS data are utilized only in the earliest observation of the relevant object, unless otherwise noted. This is to avoid the significant changes of the SIS response with time (e.g. Hwang et al. 1999).

3. Data screening and background estimation

Our strategy is to use the GIS and SIS in combination, making the best use of their characteristics. The GIS has a higher stopping power, together with a lower and stabler detector non X-ray background (NXB). In addition, the background of the GIS has been extensively studied, including both the Cosmic X-ray background (CXB) and the NXB (Ishisaki 1997, Kushino et al. 2002). Thus, the GIS data provide the principal probe with which to search for hard emission. However, the GIS is not as good as the SIS in diagnostics of soft thermal X-ray spectra, because of a lower energy resolution and a poorer low-energy quantum efficiency than those of the SIS. Therefore, we employ the SIS data in order to accurately fix the thermal IGM emission.

The data from SIS0 and SIS1 were screened with “*rev.2 standard processing*”, which selects those data taken under the cut-off rigidity higher than 6 GV, and with the source angle above the bright and night earth rim higher than 20° and 10° , respectively. We utilized the bright mode data and coadded the two (SIS0 and SIS1) spectra into a single SIS data. The background spectra were obtained from blank-sky observations, filtered through the same procedure.

Table 1. The sample objects selected for the present study.

target	position *		D †	z ‡	σ §	L_B ‖	N_H #	another name
	(α , δ)		Mpc		km s ⁻¹	10 ¹¹ L_\odot	10 ²⁰ cm ⁻²	
HCG 51	170.614,	24.294	103	0.0258	240 ^h	1.05	1.27	
HCG 62	193.277,	-9.209	58.4	0.0146	376 ⁺⁵² ₋₄₆	0.6	3.01	
HCG 97	356.844,	-2.303	87.2	0.0218	372 ^h	0.62	3.65	
NGC 507	20.901,	33.257	65.8	0.0165	595 ^w	1.73	5.24	
NGC 533	21.397,	1.772	73.7	0.0184	464 ⁺⁵⁸ ₋₅₂	0.86	3.10	
NGC 1132	43.223,	-1.275	92.8	0.0232	-	0.47	5.17	
NGC 1399	54.622,	-35.450	19.0	0.0048	374 ^d	0.45	1.34	Fornax cluster
NGC 1550	64.908,	2.410	49.6	0.0123	-	0.21	11.5	RX J0419.6+0225
NGC 2563	125.149,	21.068	59.8	0.0149	336 ⁺⁴⁴ ₋₄₀	0.55	4.23	
NGC 4325	185.796,	10.606	102	0.0257	265 ⁺⁵⁰ ₋₄₄	0.48	2.22	
NGC 5044	198.859,	-16.398	36.1	0.0090	474 ^{fs}	0.73	4.93	WP 23
NGC 5846	226.622,	1.606	24.3	0.0061	368 ⁺⁷² ₋₆₁	0.57	4.26	
NGC 6329	258.562,	43.684	110	0.0276	-	1.03	2.12	
NGC 6521	268.942,	62.604	106	0.0266	387 ^z	0.67	3.39	RX J1755.8+6236
NGC 7619	350.060,	8.206	50.1	0.0125	780 ^f	1.08	0.50	Pegasus group
Pavo	304.628,	-70.859	56.0	0.0137	169 ^{rc}	1.71	7.00	
RGH 80	200.058,	33.146	148	0.0370	467 ^r	0.32	1.05	USGC U530
S49-147	5.375,	22.402	76.0	0.0190	464 ⁺⁵⁹ ₋₂₁	1.13	4.06	

* Position of the 0.5-10 keV X-ray centroid determined from the averaged image from GIS2 and GIS3.

† Distance to the group, converted from the recession velocity listed in the NED database, assuming a Hubble constant of $H_0 = 75$ km s⁻¹ Mpc⁻¹.

‡ Redshift, from NED database.

§ Radial velocity dispersion. Groups without index are from Zabludoff, Mulchaey (1998), “h” from Hickson (1982), “d” from Drinkwater, Gregg, Colless (2001), “fs” from Ferguson, Sandage (1990), “w” from Wegner, Haynes, Giovanelli (1993), “f” from Fadda et al. (1996), “rc” from RC3 catalog (de Vaucouleurs et al. 1991), “r” from Ramella et al. (1995), and “l” from Ledlow et al. (1996).

‖ Optical B-band luminosity summed over the member galaxies of the group, obtained from RC3 catalog.

Galactic absorption column density derived from HI radio emission map by Dickey, Lockmann (1990).

Similarly, we added the data from the two GIS detectors (GIS2 and GIS3) of each observation, and further added (if multiple pointings) all observations to obtain an average GIS spectrum of each target. In order to subtract the background with the highest accuracy, in this paper we adopted the procedure used by Ishisaki (1997), rather than simply using the data from “*rev.2 standard*” screening. This method, called “H02 method”, not only employs a tighter set of data screening conditions, but also models the GIS NXB according to the distribution of counting rates of the events rejected in the on-board anti-coincidence circuit. It allows us an NXB estimation with a 1σ systematic error of 6% and 3%, for 10 ks and 40 ks observations, respectively.

To estimate the NXB in each on-source GIS dataset, the H02 method needs NXB templates. For this purpose, we prepared a data base consisting of all the GIS events detected when the ASCA telescope was pointing to the night Earth, over a period from 1993 July through 2000 July. The total exposure amounts to 5.2 Ms. All the events in the data base were sorted into 8 subsets, according to instantaneous values of “H02 scalar” which counts the GIS anti-coincidence rate. Each subset then defines a GIS background template, and the actual template to be subtracted from a particular on-source spectrum is constructed as a weighted mean of these templates. Combined with this method, we estimated the

CXB using data from 4 different blank sky regions at high galactic latitudes with $|b| > 29^\circ$, after eliminating discrete sources brighter than $\sim 2 \times 10^{-13}$ erg s⁻¹ cm⁻² in the 2–10 keV band.

In our analysis, the NXB spectra around 4-8 keV is very important. In order to further improve the accuracy of the NXB estimation, we utilize the 5.9–10.6 keV counts in the GIS detector periphery (15′ – 22′ from the detector center), hereafter denoted $N_{\text{out}}^{\text{hard}}$, to adjust residual systematic differences in the estimated and actual NXB. In calculating $N_{\text{out}}^{\text{hard}}$, we excluded a region of 3′ radius around each bright point source, and corrected $N_{\text{out}}^{\text{hard}}$ for the decrease of the detector area. About 80% of $N_{\text{out}}^{\text{hard}}$ is due to the NXB, while the remaining 20% the CXB. Any IGM signal is considered to contribute $\leq 0.1\%$ to $N_{\text{out}}^{\text{hard}}$ assuming typical spectral and spatial parameters of the IGM emission. Then, we calculated “correction factor”, as a ratio of $N_{\text{out}}^{\text{hard}}$ between the on-source data, and the background model in which the CXB contribution is fixed to those from the blank sky observations. Since a total of 80 ks exposure results in about $N_{\text{out}}^{\text{hard}} = 2000$ counts, we can estimate this factor with a statistical accuracy of $1/\sqrt{(2000)}/0.8 = 2.8\%$ (1σ).

Using the night-earth event data base utilized to construct the NXB templates, we evaluated the accuracy with which the NXB can be reproduced. The entire events in the same data base were again sorted into subsets, but this

Table 2. Log of the ASCA observations utilized in the present work.

target	r*	sequence ID [†] (year)	exposure [‡]	
			GIS	SIS
HCG 51	10'	82028000('94) ^{s2}	62	72
HCG 62	15'	81012000('94) ^{s2} , 86008000('98), 86008010('98), 86008020('98), 86008020('98)	121	29
HCG 97	10'	84006000('96) ^{s1}	79	81
NGC 507	15'	61007000('94) ^{s2§} , 61007010('95), 63026000('95) ^o	80	25
NGC 533	10'	62009000('94) , 62009010('96) ^{s2}	35	18
NGC 1132	10'	65021000('97) ^{s1}	27	20
NGC 1550	15'	87005000('99) ^{s1}	70	23
NGC 1399	20'	80038000('93) ^{s4} , 80039000('93), 81021000('94) ^o , 87006000('99) ^o , 87006010('99) ^o , 87006020('99) ^o , 87006030('99) ^o , 87006040('99) ^o	145	17
NGC 2563	12'	63008000('95) ^{s1}	46	52
NGC 4325	10'	85066000('97) ^{s2}	27	25
NGC 5044	15'	80026000-10('93) ^{s4} , 87002000('99) ^o , 87002010('99) ^o , 87002020('99) ^o , 87002030('99) ^o	111	19
NGC 5846	15'	61012000('94) ^{s4}	36	28
NGC 6329	12'	84047000('96) ^{s2}	37	34
NGC 6521	10'	85034000('97) ^{s1}	36	19
NGC 7619	12'	63017000('95) ^{s2}	56	59
Pavo	10'	81020000('94) ^{s4}	29	26
RGH 80	10'	83012000('95) ^{s2} , 93007040('95) ^o , 93007080('95) ^o , 93007070('95) ^o	67	42
S49-147	15'	81001000('93) ^{s4}	32	29

* Radius of the spectral integration region.

† Observation IDs. The SIS data are extracted only from the observations with “s”. Associated number represents the CCD mode, such as 1, 2 and 4 CCD modes. Offset pointing are labeled as “o”.

‡ The total effective exposure of the observation, including the offset pointings.

§ The data only from the SIS0 is used. The shape of the SIS1 spectra was odd, and inconsistent with the short supplemental observation (ID=61007010).

|| The SIS data from the first observation is not used. The CCD temperature was too high for the 4 CCD mode operation and the shape of the spectra is severely distorted and unreliable (e.g. Finogenov et al. 2002).

time, with each subset covering one month. The monthly exposure scatters between 18 ks and 150 ks, with an average of 85 ks; those months with the exposure less than 40 ks were discarded. From each monthly-accumulated night Earth spectrum, we subtracted the template background synthesized in the same way as before using the H02 method with the correction using $N_{\text{out}}^{\text{hard}}$. (Each monthly spectrum and the template are both derived from the same data base, but using different sortings.) Figure 2 shows the ratio of the count rate of each monthly spectrum, to that dictated by the synthesized template. While the $N_{\text{out}}^{\text{hard}}$ correction utilizes the 5.9–10.6 keV band, the comparison in figure 2 (left) is carried out in the 4–8 keV band, which is used in the following sections to search for excess hard X-ray emission. Including the statistical error of the 4-8 keV counts, our method provides an rms scatter of 3.3%, which is better than what is achieved by the original H02 method alone (4.0%).

In figure 2 (left), the ratio exhibits a gradual decrease by about 1-2%, after the month 66 (1999 July); this is due to orbit decay of ASCA, as is clear from figure 2 (right). By representing this trend by two linear segments as shown by a dashed line in the figure, the reproducibility of our NXB estimation method was improved to 3.0%. In the following analysis, the systematic error in the NXB estimation in each target is defined as a quadrature sum of the statistical error associated with $N_{\text{out}}^{\text{hard}}$, and a 1% systematic error representing any residual unknown factors.

4. Data Analysis and Results

4.1. X-ray images

Figure 3 and figure 4 show 0.5–10 keV GIS images of the 18 objects, obtained after subtracting the background (NXB and CXB) as derived above. Every object thus exhibits diffuse IGM emission with a roughly circular profile, which is detected up to a radius of 10' – 25'. The X-ray centroid is generally coincident in position with a bright (often the brightest) elliptical galaxy in the system. For each object, we then defined a spectral integration region, as indicated in these figures (dashed circles) and listed in table 2. These regions are fully covered by the GIS, but only partially by the SIS. We eliminated regions around bright contaminating sources, such as the NGC 1404 galaxy close to NGC 1399 and the NGC 499 galaxy near NGC 507. Similarly, we removed regions of 3' radius around point sources in the 2RXP catalog¹, if their 0.1–2.5 keV count rates are higher than 4×10^{-3} counts s⁻¹. From independent analysis using our GIS data, the 2–10 keV fluxes of these sources are confirmed to be $\lesssim 2 \times 10^{-13}$ erg s⁻¹ cm⁻². Positions of all removed sources are also presented in figure 4.

4.2. Basic characteristics of the X-ray spectra

In this section, we present the GIS and SIS spectra of our sample objects, and quantify them through spectral

¹ <http://wave.xray.mpe.mpg.de/rosat/rra/rospspc>

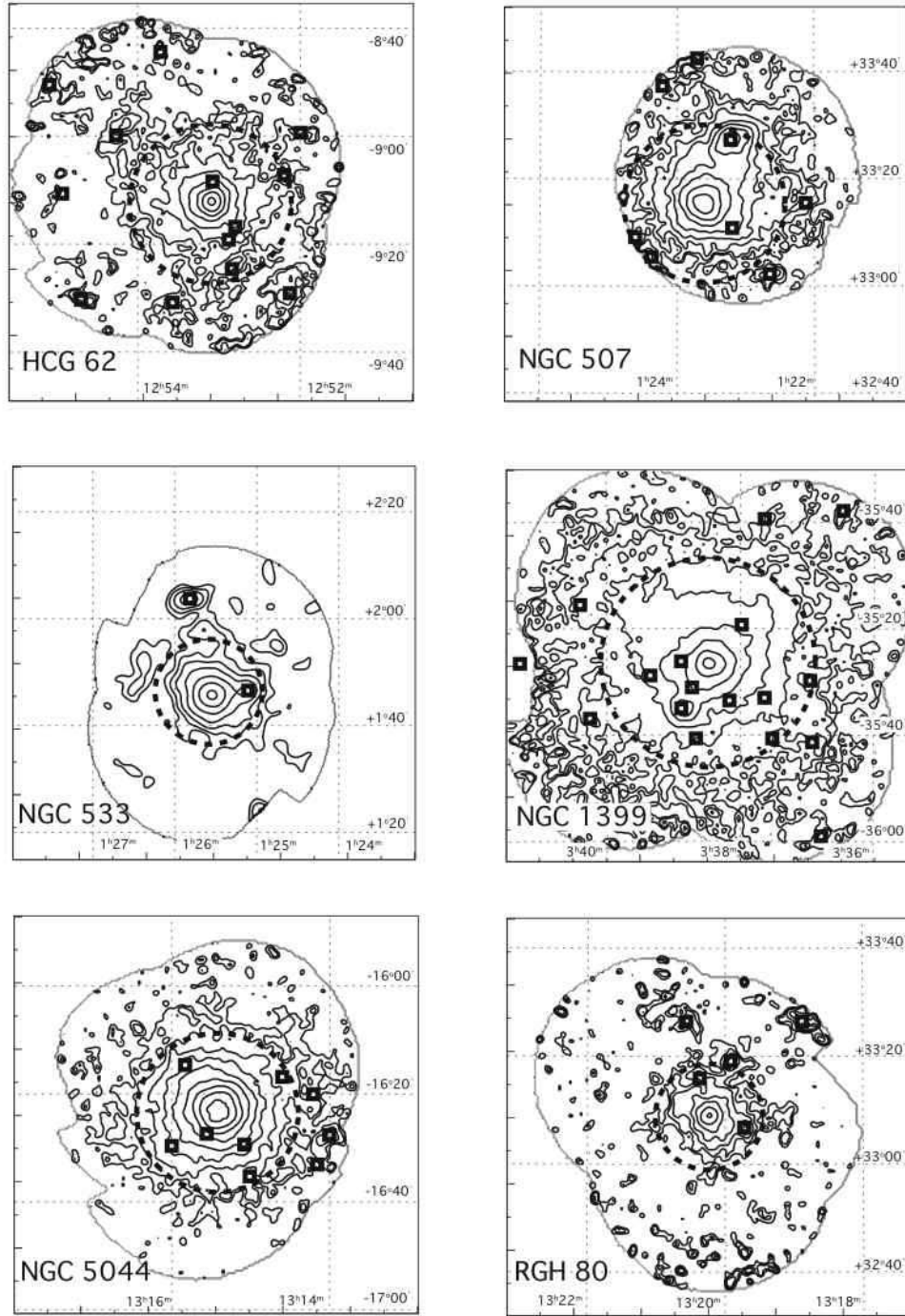


Fig. 3. Background-subtracted 0.5–10 keV GIS (GIS2 plus GIS3) mosaic images of the groups of galaxies in the present sample, observed under multiple pointings. Each image is corrected for overlapping exposure, and is smoothed by a Gaussian function with $\sigma = 1'$. Contours are logarithmically spaced with a factor of 1.7, starting from 3×10^{-5} cts $s^{-1} \text{ cm}^{-2} \text{ arcmin}^{-2}$. In NGC 1399 and NGC 5044, the least significant contour is deleted for simplicity. The gray thin line indicates the combined GIS field of view. Dashed circle shows the region used for spectral accumulation. Boxes represent point sources eliminated in the spectral analysis.

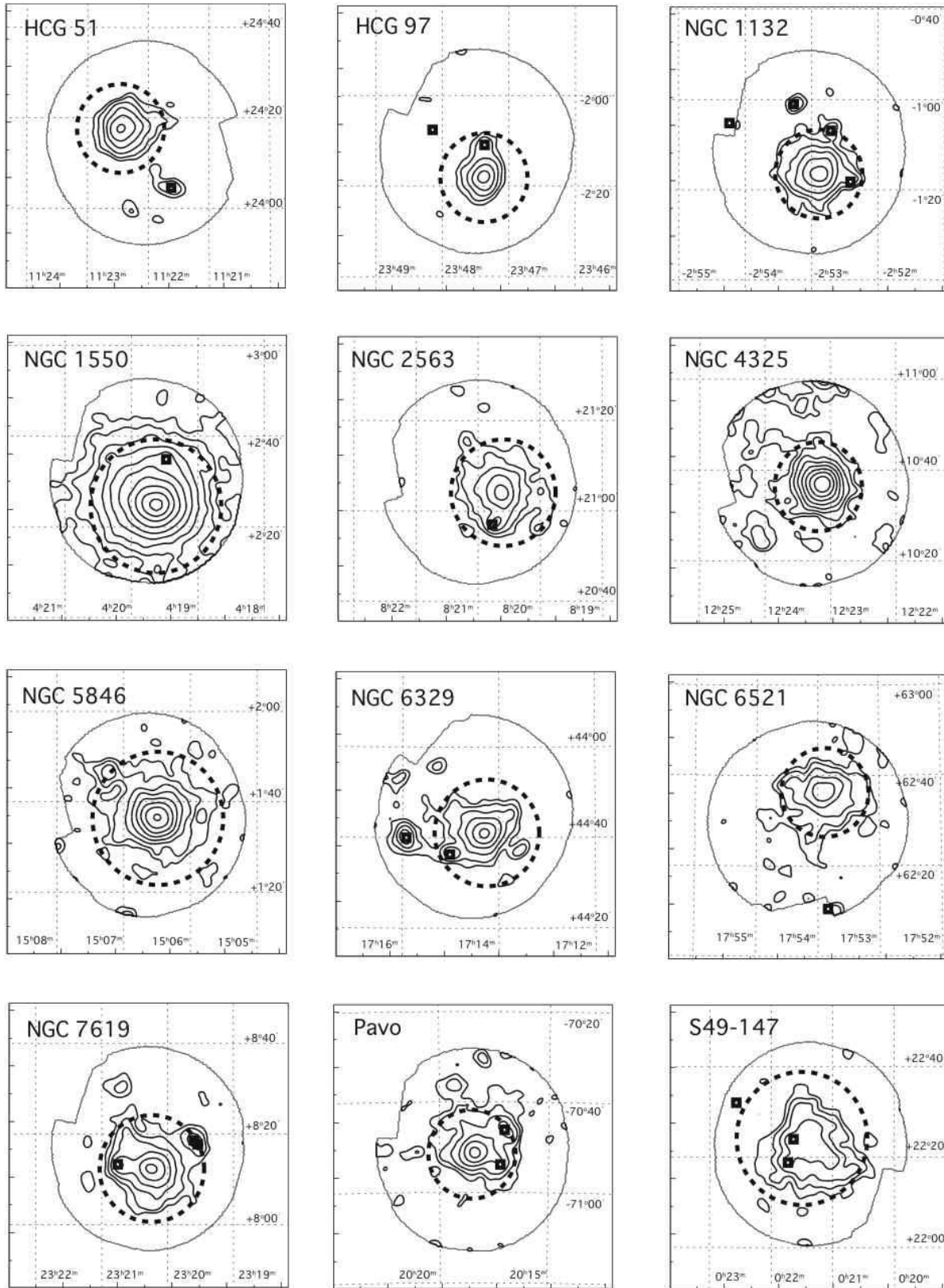


Fig. 4. The same as figure 3, but for the groups with single pointing.

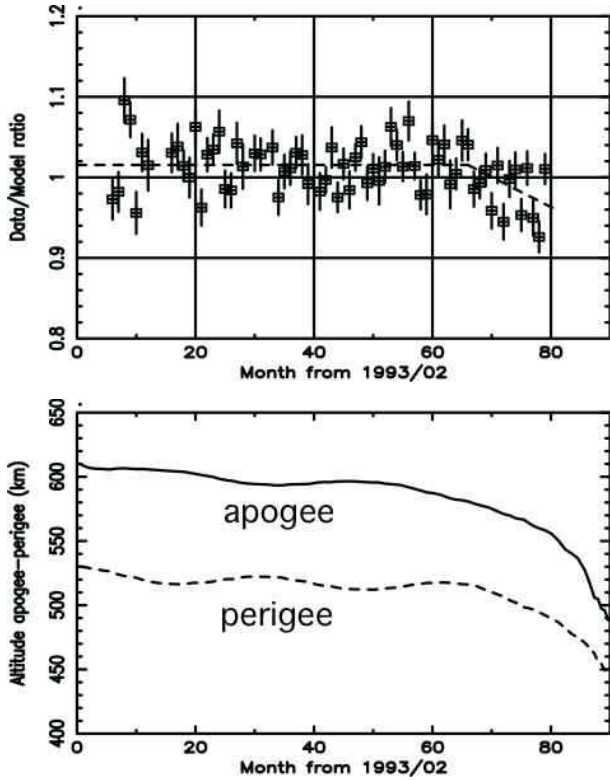


Fig. 2. (left) The 4-8 keV GIS counting rate in the $r < 15'$ region averaged over each month, normalized to the background modeled with our method. See text for detail. The dashed line is an analytic model fit. (right) Changes of the apogee and perigee heights of ASCA.

model fittings. A particular care is needed here, because the soft part and hard part (typically below and above ~ 2.5 keV, respectively) of the spectra are subject to distinct sources of errors. Obviously, the hard-band data are strongly affected by the statistical and background uncertainties. In contrast, the soft-band spectra have such high signal statistics that their uncertainties are dominated by those in the instrumental responses rather than in the background. Given these, we first quantify the IGM emission using the soft-band spectra, and then examine whether the results can explain the hard-band data or not.

4.2.1. Fitting procedure

Figure 5 shows background-subtracted GIS (black) and SIS (red) spectra of our 18 targets, derived from the spectral accumulation regions defined above. The GIS background has been subtracted as detailed in section 3, while the SIS background using blank-sky observations (also section 3). Errors associated with the GIS data points include the systematic background uncertainties noted in section 3. In contrast, those assigned to the SIS spectra are statistical only, because in this case Poisson errors of the signal and background counts are dominant, in softer and harder energies, respectively. The SIS spectra thus reveal Fe-L, Mg-K, and Si-K lines, indicating the dominance of thermal IGM emission, whereas the GIS signals

are generally detectable to energies beyond ~ 5 keV.

Below, we apply various spectral models simultaneously to the GIS and SIS spectra of each object, utilizing energies above 1.0 keV and 0.7 keV, respectively. To handle the difference between the GIS and SIS fields of view, the model normalization (of individual components if the model is composite) is allowed to differ between the two instruments. When dealing with optically-thin thermal emission models, we classify major heavy elements into two groups in view of their origin (e.g., Matsushita 1997); one group comprises O, Ne, Na, Mg, Al, Si, S, Ar and Ca, which are mainly so-called α -elements, while the other group consists of Fe and Ni. Abundances of the first and second metal groups are denoted as Z_α and Z_{Fe} , respectively. For the IGM emission calculations, we used both the vMEKAL and vAPEC codes provided by the XSPEC package. Since the two models give only minor differences, below we refer only to the vMEKAL results. The absorption column density was fixed to the value derived from HI observations (Dickey, Lockman, 1990). These parameters are also listed in table 1.

The SIS and GIS responses have some residual uncertainties, which are dominated by their gain calibration errors as a function of the detector position; we quote those of the SIS and GIS as $\sim 0.5\%$ and $\sim 1\%$, respectively². In some of the brightest objects in our sample, however, these values turned out to be insufficient to fully represent the instrumental calibration uncertainties in the soft energy band where the signals have very high statistics. As a conventional way to solve this problem, we allowed the model red-shift parameter to vary independently within $\pm 0.5\%$ and $\pm 1\%$, for the SIS and the GIS, respectively, from that taken from the NED data base³. When analyzing the SIS data taken in the 4-CCD mode, the SIS gain tolerance was slightly relaxed to $\pm 1\%$, to incorporate additional gain uncertainties.

For the NGC 1550 group, we set free the absorption column of the SIS data, because the earliest data of this group was obtained in 1999 when the SIS degradation had already been significant; the additional absorption is expected to emulate changes in the SIS response (e.g. Hwang et al. 1999). For the NGC 6329 group, we limited our analysis to energies above 0.85 keV for the SIS. This is because a significant soft hump is observed below this energy, which is not detected by, e.g., ROSAT (e.g. Mukchaey et al. 2003) and supposed to be instrumental. Even if the humps is included in the fit, it requires very soft ($kT < 0.1$ keV) component, which does not affect the results in the following sections.

4.2.2. Single-temperature fits to the soft-band spectra

As the first attempt, we applied a common vMEKAL model to the GIS and SIS spectra of each object, over a limited soft energy range below 2.5 keV. The results are summarized in table 3, and the obtained best-fit models are shown as a histogram in figure 5. There, the models determined in the energy range below 2.5 keV are extrapo-

² http://heasarc.gsfc.nasa.gov/docs/asca/cal_probs.html

³ <http://nedwww.ipac.caltech.edu/>

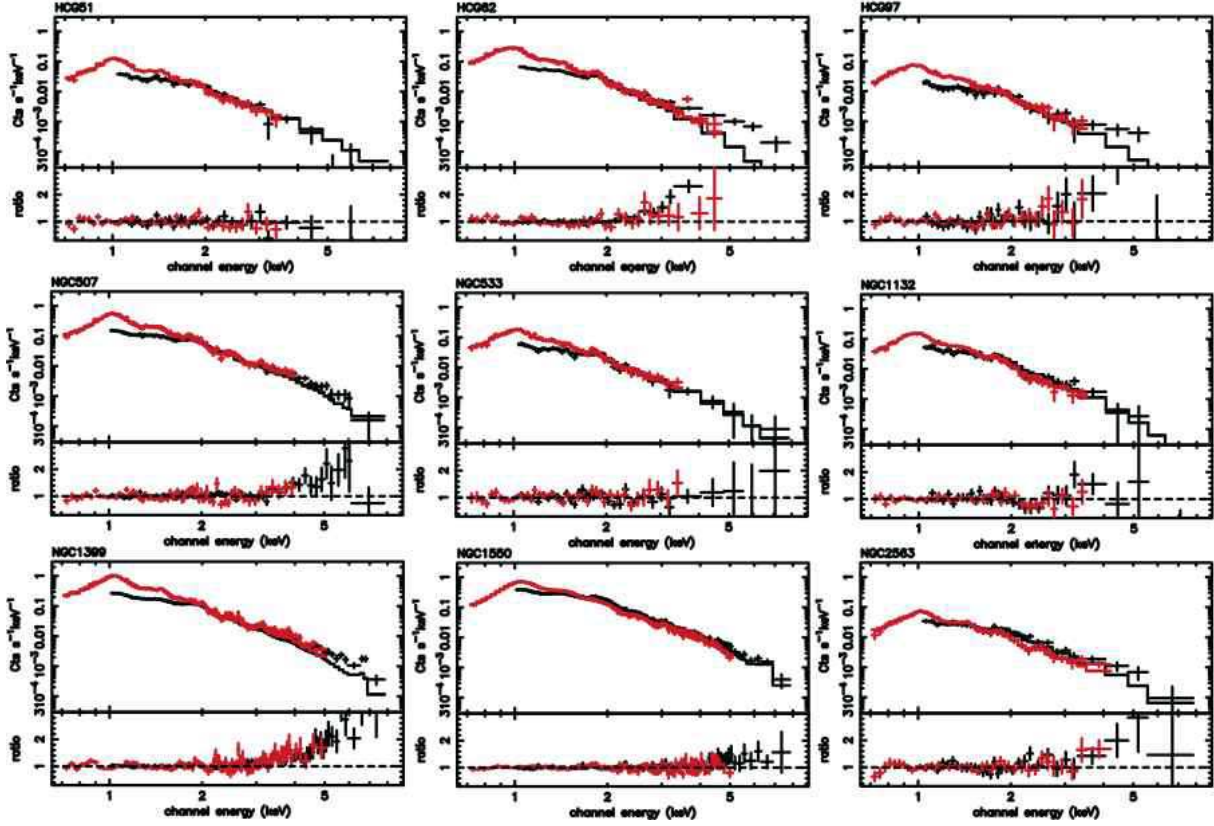


Fig. 5. The GIS (black) and SIS (red) spectra of our sample objects, jointly fitted with a vMEKAL model in the energy below 2.5 keV. The models are extrapolated to higher energies. All spectra are plotted to the same scale.

lated to higher energies, to be compared with the observed data. These soft-band fits gave the IGM temperature in the range $kT_S = 0.7 - 1.7$ keV, together with sub-solar metal abundances. The 0.7–2.5 keV band flux, F_{soft} , was obtained in the range of $1 - 20 \times 10^{-12}$ erg s $^{-1}$ cm $^{-2}$.

In nearly half the objects, the single-temperature fits are in fact formally unacceptable. In NGC 507, NGC 1399, NGC 1550, NGC 5044, NGC 5846, and Pavo, the fit leaves significant residuals around atomic emission lines. This suggests that their spatially-integrated IGM emission cannot be described adequately with single-temperature thermal models: later in section 4.2.4, we hence introduce two-temperature models.

In figure 5, we also notice that the data at energies above ~ 3 keV often exceed the model extrapolation, in at least 6 objects such as HCG 62, NGC 507, NGC 1399, and RGH 80. This suggests the presence of additional harder emission components in these objects. Actually, if we fit the GIS/SIS spectra of these objects over the whole energy band including data points above 2.5 keV, the reduced chi-squared further increases by ~ 0.3 or more.

4.2.3. Properties of the hard-band spectra

In order to characterize the spectra in the hard band, we next analyzed the 2.5–8 keV GIS data of our sample objects. The SIS data were not incorporated, since the SIS background systematics above 2.5 keV is not well understood. We employed the same single-temperature

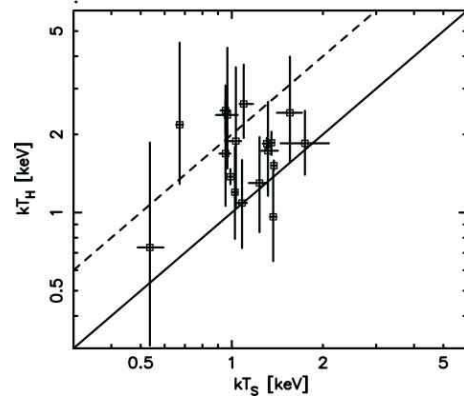


Fig. 6. The best fit temperature from the hard-band fitting (kT_H), compared to that from the soft-band fitting (kT_S). Statistical 90% errors are plotted. The solid line indicates $kT_H = kT_S$, while the dashed line $kT_H = 2kT_S$.

vMEKAL model, but fixed Z_α and Z_{Fe} both to 0.5 solar for simplicity, because this energy range is relatively devoid of strong metal lines when the plasma temperature is $\lesssim 2$ keV. The red-shift is also fixed at the optical value. Then, the temperature in this energy range, denoted kT_H , is to be determined by the continuum shape.

Since the GIS data above 2.5 keV are dominated by the background (NXB+CXB), errors associated with kT_H in

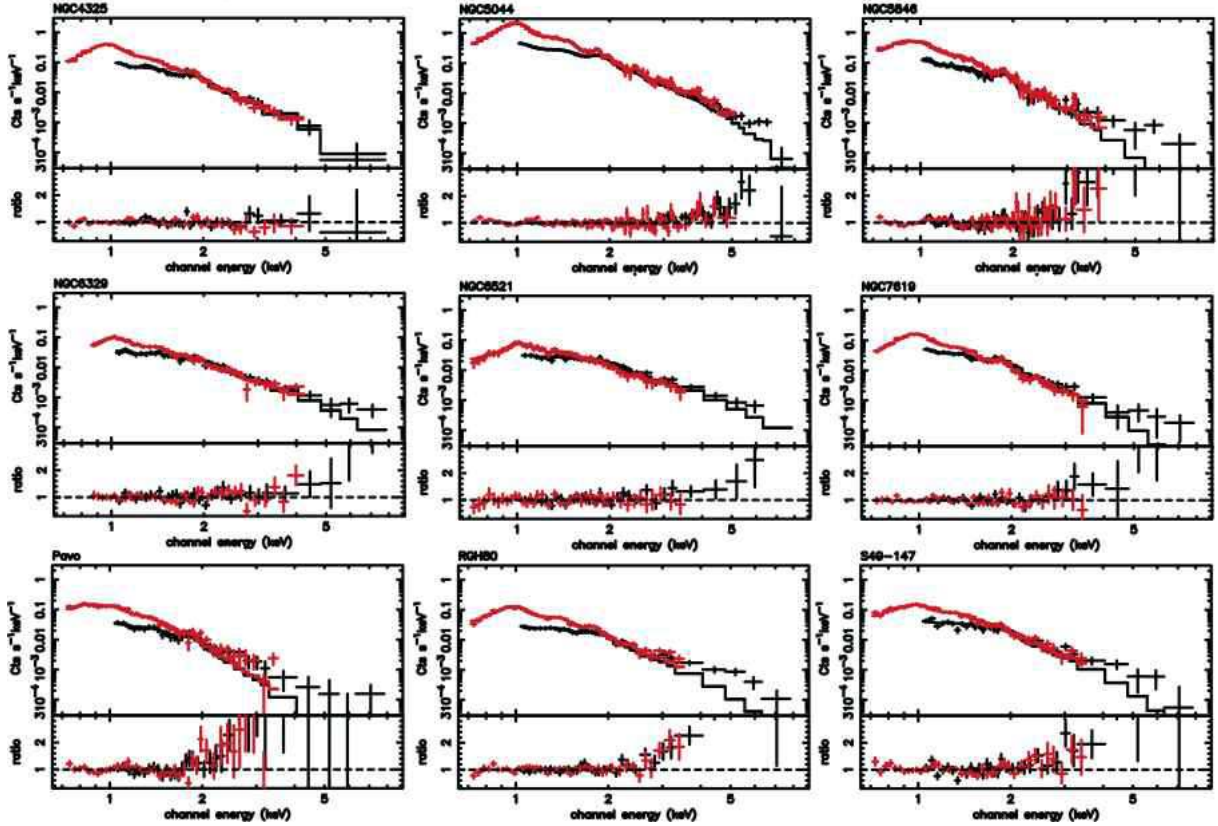


Fig. 5. (continued)

this case are expected to come from three major sources; photon counting statistics, systematic errors in the NXB subtraction, and those of the CXB. The formal “fitting error” takes into account the first two factors, because the NXB estimation errors are already included in the error bars of individual GIS data points (section 4.2.1). However, the third factor is not. Accordingly, we estimated the CXB contribution as described in the end of this subsection, and present them in addition to the fitting errors for kT_H .

The hard-band temperatures kT_H , obtained in this way, are listed in table 3, and are compared in figure 6 with the soft-band temperature kT_S . Although the errors (taking into account all the three sources) are large, we find that kT_H is generally higher than kT_S , even reaching $\sim 2kT_S$ in some objects (e.g., HCG 62 and RGH 80). This result reinforces the positive data excess toward higher energies, which are suggested by figure 5. For reference, the obtained kT_H does not change significantly even if the 2.5–4.0 keV SIS data are included to the fit.

The third factor causing errors in kT_H , namely sky-to-sky fluctuations in the CXB surface brightness I_{CXB} , occurs as the number of faint objects that constitute the CXB fluctuates. Assuming a simple Euclidean log N -log S relation as $N(>S) \propto S^{-1.5}$, where S is the source flux and $N(>S)$ is the number of sources with fluxes higher than S , the CXB brightness fluctuation σ_{CXB} is described as $\sigma_{\text{CXB}}/I_{\text{CXB}} \propto \Omega_e^{-0.5} S_c^{0.25}$. Here, S_c is the upper flux

bound of the individually eliminated sources, which is $\sim 2 \times 10^{-13}$ erg s $^{-1}$ cm $^{-2}$ (2–10 keV) in this analysis, and Ω_e is the effective solid angle of the detector. For the ASCA GIS, Ω_e has been calculated by Ishisaki (1997), by taking into account the ASCA vignetting function. In the present case, a typical data accumulation radius of 15' gives $\Omega_e = 0.1$ deg 2 . By scaling the HEAO-1 A2 result (Shafer, Fabian 1998) with these values, we typically find that the 2.5–8 keV CXB fluctuates from field to field by 7.9% (1σ) in the present case. Then, by fitting the GIS spectra with the CXB level artificially changed (by a level corresponding to the 90% range of its fluctuation), we evaluated the error propagation from the CXB brightness to kT_H .

4.2.4. Two-temperature IGM modeling

The single-temperature vMEKAL fit to the soft band spectra ended up unacceptable in 10 objects (section 4.2.2): before examining the hard excess suggested by the large difference between kT_S and kT_H in several objects, we need to arrive at an acceptable IGM modeling of all objects. These fit failures are most likely caused by their slight deviation from the assumed isothermality, because temperature gradients in the X-ray emitting plasma are rather common among groups and clusters of galaxies. Even in such a case, two temperatures are generally known to be sufficient to describe the integrated X-ray spectrum (e.g., Fukazawa 1997).

We applied a two-temperature vMEKAL model (2-

Table 3. Results of the joint fit to the GIS and SIS spectra below 2.5 keV with a single component vMEKAL model.

target	kT_S^*	Abundance †		χ^2/dof	F_{soft}^\ddagger	kT_H^\S	note $^\parallel$
	(keV)	$Z_\alpha(Z_\odot)$	$Z_{\text{Fe}}(Z_\odot)$				
HCG 51	1.37 $^{+0.03}_{-0.03}$	0.44 $^{+0.15}_{-0.12}$	0.36 $^{+0.07}_{-0.05}$	72.0/52	1.9	0.96 $^{+0.50+0.74}_{-0.31-0.41}$	*
HCG 62	0.95 $^{+0.03}_{-0.04}$	0.31 $^{+0.09}_{-0.07}$	0.15 $^{+0.03}_{-0.03}$	70.0/52	4.0	2.47 $^{+0.61+0.55}_{-0.46-0.57}$	*
HCG 97	1.03 $^{+0.04}_{-0.06}$	0.31 $^{+0.16}_{-0.12}$	0.19 $^{+0.05}_{-0.04}$	59.5/52	0.9	1.88 $^{+1.74+1.29}_{-0.84-1.15}$	
NGC 507	1.35 $^{+0.03}_{-0.03}$	0.62 $^{+0.12}_{-0.10}$	0.41 $^{+0.06}_{-0.05}$	128.8/96	7.8	1.86 $^{+0.19+0.17}_{-0.19-0.19}$	*
NGC 533	1.23 $^{+0.08}_{-0.10}$	0.52 $^{+0.26}_{-0.18}$	0.31 $^{+0.11}_{-0.08}$	80.7/52	2.7	1.30 $^{+0.65+0.66}_{-0.46-0.57}$	**
NGC 1132	1.08 $^{+0.04}_{-0.04}$	0.33 $^{+0.15}_{-0.11}$	0.27 $^{+0.06}_{-0.05}$	53.9/52	2.7	1.09 $^{+0.51+0.48}_{-0.36-0.37}$	
NGC 1399	1.31 $^{+0.02}_{-0.04}$	0.56 $^{+0.03}_{-0.06}$	0.35 $^{+0.03}_{-0.04}$	239.9/104	14.3	1.84 $^{+0.09+0.09}_{-0.11-0.11}$	**
NGC 1550	1.38 $^{+0.02}_{-0.02}$	0.58 $^{+0.07}_{-0.06}$	0.42 $^{+0.04}_{-0.03}$	191.9/103	19.1	1.52 $^{+0.07+0.09}_{-0.06-0.08}$	**
NGC 2563	1.32 $^{+0.10}_{-0.07}$	0.64 $^{+0.31}_{-0.21}$	0.28 $^{+0.14}_{-0.07}$	45.7/52	1.6	1.73 $^{+0.94+0.84}_{-0.57-0.80}$	
NGC 4325	1.02 $^{+0.02}_{-0.02}$	0.42 $^{+0.16}_{-0.12}$	0.32 $^{+0.07}_{-0.05}$	61.0/52	4.6	1.20 $^{+0.60+0.59}_{-0.41-0.43}$	
NGC 5044	0.99 $^{+0.01}_{-0.01}$	0.39 $^{+0.04}_{-0.04}$	0.27 $^{+0.02}_{-0.02}$	261.3/104	23.4	1.36 $^{+0.11+0.12}_{-0.11-0.12}$	**
NGC 5846	0.67 $^{+0.02}_{-0.02}$	0.40 $^{+0.20}_{-0.11}$	0.18 $^{+0.05}_{-0.03}$	136.8/98	7.0	2.18 $^{+2.34+1.24}_{-0.89-1.21}$	**
NGC 6329	1.56 $^{+0.15}_{-0.15}$	0.63 $^{+0.43}_{-0.29}$	0.39 $^{+0.22}_{-0.17}$	38.2/47	1.6	2.42 $^{+1.56+0.92}_{-0.86-1.00}$	
NGC 6521	1.74 $^{+0.35}_{-0.29}$	0.69 $^{+0.45}_{-0.33}$	0.38 $^{+0.24}_{-0.18}$	36.5/52	1.6	1.85 $^{+0.62+0.50}_{-0.45-0.49}$	
NGC 7619	0.95 $^{+0.04}_{-0.04}$	0.42 $^{+0.15}_{-0.13}$	0.23 $^{+0.05}_{-0.05}$	55.9/52	2.7	1.69 $^{+1.00+0.96}_{-0.63-0.92}$	
Pavo	0.54 $^{+0.06}_{-0.05}$	0.17 $^{+0.18}_{-0.10}$	0.06 $^{+0.02}_{-0.03}$	70.1/52	1.9	0.73 $^{+1.13+1.30}_{-0.43-0.36}$	*
RGH 80	1.09 $^{+0.08}_{-0.03}$	0.50 $^{+0.17}_{-0.14}$	0.18 $^{+0.04}_{-0.03}$	50.9/52	1.3	2.62 $^{+1.09+0.77}_{-0.68-0.79}$	
S49-147	0.97 $^{+0.08}_{-0.08}$	0.15 $^{+0.09}_{-0.08}$	0.06 $^{+0.02}_{-0.02}$	81.7/52	2.2	2.38 $^{+1.94+0.83}_{-0.90-0.87}$	**

* Best fit temperature in the energy band below 2.5 keV.

† Best fit metal abundances in the energy band below 2.5 keV.

‡ Flux in the energy band from 0.7 to 2.5 keV (10^{-12} erg s $^{-1}$ cm $^{-2}$).

§ Best fit temperature from the hard-band fitting, above 2.5 keV. Errors are the 90% statistical and systematic ones.

$^\parallel$ Targets in which the soft-band fitting is not statistically acceptable in 90% and 99% confidence are indicated with "*" and "**", respectively.

vMEKAL model) to the GIS and SIS spectra of the 10 objects, again in the energy range below 2.5 keV. The two vMEKAL components were allowed to take free temperatures and normalizations, but were constrained to have the same abundance parameters. To avoid strong couplings between them, we constrained the hotter temperature (kT_2) to stay between 0.8 and 25 keV; the former is a typical cooler component temperature kT_1 , while the latter is 10 times the upper bound of the employed energy range.

Results of the 2-vMEKAL fits are summarized in table 4. Spectra of HCG 62, NGC 5846 and Pavo have been fitted successfully by the 2-vMEKAL model when the abundances are grouped as Z_α and Z_{Fe} . When the abundances of Mg, Al, Si, and S are set free, S49-147 gave acceptable fit. With the same model, HCG 51, NGC 507 and NGC 533 gave marginally (at 99% confidence) acceptable fits, although kT_2 is not well determined in the latter two objects.

The remaining 3 objects (NGC 1399, NGC 1550 and NGC 5044) have such high statistics around 1 keV that the fits remained still unacceptable even setting the Mg, Al, Si, S abundances free. However, the fit itself has greatly improved by adding the second component, implying that their spectra clearly prefer the 2-vMEKAL model to the vMEKAL model. Adding a third emission component does not improve the fit significantly. The fit failure in these objects is partially due to slight discrepancy between the SIS and the GIS data, at ~ 1.2 keV and

~ 2.1 keV, presumably due to calibration errors. (The same features are often present in other observations, but usually negligible compared to data statistics.) We hence decided to simply ignore the energy bands of 1.15–1.25 keV and 2.1–2.2 keV. Then the fit improved significantly, and became marginally acceptable by 99% in NGC 1399 and NGC 1550, while still unacceptable by 99.6% in NGC 5044.

4.3. Excess Hard X-ray Signals

Having fixed the IGM emission using the soft-band data, let us examine the significance of the suggested excess hard X-ray emission by counting excess photons, employing the energy band from 4 to 8 keV. In this range, the GIS still has an effective area of 40–80 cm 2 , but contribution from the IGM emission is expected to be very small. In fact, 70–99 % of the raw count rate in this band is from the background, of which the CXB and the NXB have comparable shares.

In table 5, the 3rd column represents the raw (background inclusive) 4–8 keV GIS count rate of each object accumulated over the specified data integration region (figure 3 and figure 4), together with the purely statistical 1σ errors. The 4th column shows the expected CXB contribution, of which the errors refer to 1σ sky-to-sky fluctuation calculated in the same way as in section 4.2.3 (e.g., 7.9% for a region of 15' in radius). The 5th column represents the estimated NXB count rate, derived as described in section 3. Since the NXB templates have high photon

Table 4. Results of the 2-vMEKAL model fitting in energies below 2.5 keV .

target	Model*	kT_1^\dagger (keV)	kT_2^\ddagger (keV)	Abundance $Z_{\text{Fe}}(Z_\odot)$	χ^2/dof	note [§]	$-\Delta\chi^2^\parallel$
HCG 51	6Z	$0.98^{+0.15}_{-0.23}$	$1.76^{+0.51}_{-0.38}$	$0.70^{+0.60}_{-0.33}$	59.7/45	*	(12.3)
HCG 62	2Z	$0.78^{+0.07}_{-0.23}$	$1.27^{+0.33}_{<0.80}$	$0.24^{+0.08}_{-0.07}$	50.6/49		19.4
NGC 507	6Z	$0.71^{+0.70}_{-0.29}$	$1.36^{>25.0}_{-0.07}$	$0.46^{+0.33}_{-0.11}$	109.7/86	*	(19.1)
NGC 533	6Z	$1.12^{+0.11}_{-0.78}$	$1.42^{+1.52}_{<0.80}$	$0.34^{+0.16}_{-0.08}$	68.1/45	*	(12.6)
NGC 1399	6Z-	$0.82^{+0.07}_{-0.14}$	$1.43^{+0.17}_{-0.10}$	$0.44^{+0.14}_{-0.05}$	107.4/79	*	33.5
NGC 1550	6Z-	$0.95^{+0.33}_{-0.35}$	$1.44^{+0.14}_{-0.10}$	$0.52^{+0.40}_{-0.14}$	105.9/78	*	(15.9)
NGC 5044	6Z-	$0.67^{+0.09}_{-0.11}$	$1.11^{+0.05}_{-0.05}$	$0.35^{+0.05}_{-0.02}$	116.7/79	**	61.0
NGC 5846	2Z	$0.63^{+0.02}_{-0.02}$	$1.28^{+0.07}_{-0.45}$	$0.36^{+0.04}_{-0.07}$	92.3/92		44.5
Pavo	2Z	$0.39^{+0.09}_{-0.07}$	$1.56^{+0.84}_{-0.24}$	$0.58^{+8.35}_{-0.37}$	40.9/49		29.2
S49-147	6Z	$0.60^{+0.19}_{-0.60}$	$1.15^{+0.21}_{<0.80}$	$0.09^{+0.06}_{-0.05}$	54.3/45		27.4

* Model ID. “2Z” means that the abundances are grouped into two (Z_α and Z_{Fe}). “6Z” means models with Mg, Al, Si and S set free, in addition to “2Z”. “6Z-” means after subtracting the two energy bands. See text.

† Temperature of the cooler component.

‡ Temperature of the hotter component. Parameters hitting the limit (0.8–25 keV) are presented with > or <.

§ Targets in which the soft-band fitting is not statistically acceptable in 90% and 99% confidence are indicated with “*” and “**”, respectively.

∥ Improvement in χ^2 by introducing the second thermal component. Presented with parentheses, if the improvement is not significant with F-test by 1%.

statistics (section 3), the quoted errors are 1σ systematic, which is typically 3.2 % and 2.0% for 40 ks and 120 ks observations, respectively. The 6th column gives the IGM contribution to the 4–8 keV band, calculated by extrapolating the soft-band determined IGM model. We used the 1-vMEKAL fit if it is acceptable, whereas the 2-MEKAL fit otherwise. Although uncertainties in the IGM contribution have composite origin, they are dominated by statistical errors in the soft-band temperature determination, because the error is amplified as the model prediction is extrapolated toward the higher 4–8 keV range. We hence calculated how the errors associated with the soft-band temperature determinations propagate into those in the 4–8 keV counts. The original 90% confidence errors were convert into 1σ values assuming a Gaussian distribution.

The 7th column in table 5 lists the 4–8 keV excess count rates of the 18 objects, derived by subtracting the CXB, NXB, and IGM from the raw data. There, the statistical and systematic errors are given separately; the former comes from that of the raw data, while the latter is the quadrature sum of those associated with the three components subtracted. The last column represent significance of the excess counts, calculated against the overall uncertainty which is the quadrature sum of the statistical and systematic errors. These values are also presented in figure 7. Thus, the hard-band excess above the soft-band determined IGM model is insignificant ($\lesssim 1\sigma$ level) in 10 out of the 18 objects, and is marginal ($\sim 1.5\sigma$ level) in 4 objects (NGC 1550, NGC 5846, NGC 6329 and S49-147). In contrast, the significance is higher than 2σ in 3 groups of galaxies, namely HCG 62, NGC 1399, and RGH 80. Among them, the soft band IGM modeling of the first and the last objects is statistically acceptable. In the case of NGC 1399, the somewhat poor IGM modeling (acceptable at 98%) hampers us to draw a firm conclusion, but

the hard excess could also be present because its nominal significance is rather high (4σ). Properties of these 3 objects are discussed in detail in the next sub-section.

The NGC 5044 group also shows excess significance as 2.6σ . The IGM modeling in this source, however, is unacceptable even by 99% confidence (with $\chi^2/\text{dof} = 116.7/79$), so that the errors associated with the IGM contribution could be underestimated. In addition, the excess hard emission itself is weak. We estimated the 2–10 keV hard band flux F_{hard} assuming a power-law model with photon index Γ fixed at 2.0, from the excess hard counts in table 5. The value of F_{hard} thus obtained amounts to only 4% of the F_{soft} . Thus, we conclude that the hard excess signal suggested in NGC 5044 is not significant enough in this study.

4.4. Detailed analysis of selected objects

In this section, we analyze in detail the 3 objects, HCG 62, NGC 1399 and RGH 80, which have been found in section 4.3.2 to require a significant hard X-ray component, in addition to the thermal IGM model (either vMEKAL or 2-vMEKAL). As already reported by Fukazawa et al. (2001), the compact group HCG 62 shows the strong excess signal, and the IGM contribution to its 4–8 keV excess counts is only $\sim 25\%$. Therefore, this object provides an ideal benchmark test for our work, particularly in comparison with Fukazawa et al. (2001). We study RGH 80 as well, because it also shows evidence of strong hard excess signal, including the high value of $kT_{\text{H}} = 2.62$ keV. In the case of NGC 1399, the soft band IGM modeling is only marginally acceptable and also the value of kT_{H} is less than 2 keV, while the excess is still significant in the previous analysis. Thus, this objects also requires detailed analysis.

Table 5. Excess rates in the 4-8 keV band with IGM contribution calculated below 2.5 keV.

target	Model*	Data [†]	CXB [‡]	NXB [§]	IGM	Excess [#]	Sigma**
HCG 51	2T	10.96 ± 0.30	6.12 ± 0.73	4.76 ± 0.12	1.15 ± 0.45	1.07 ± 0.30 ± 0.87	-1.17
HCG 62	2T	20.26 ± 0.29	8.24 ± 0.66	9.21 ± 0.18	0.81 ± 0.15	2.00 ± 0.29 ± 0.70	2.64
HCG 97	1T	11.46 ± 0.27	5.50 ± 0.66	5.48 ± 0.13	0.17 ± 0.01	0.32 ± 0.27 ± 0.67	0.44
NGC 507	2T	20.91 ± 0.36	7.42 ± 0.59	8.97 ± 0.21	3.07 ± 1.54	1.45 ± 0.36 ± 1.66	0.85
NGC 533	2T	12.01 ± 0.42	5.76 ± 0.69	5.28 ± 0.17	0.55 ± 0.09	0.42 ± 0.42 ± 0.72	0.51
NGC 1132	1T	10.21 ± 0.43	5.64 ± 0.68	4.53 ± 0.17	0.52 ± 0.03	-0.48 ± 0.43 ± 0.70	-0.58
NGC 1399	2T	26.75 ± 0.30	8.68 ± 0.52	9.84 ± 0.18	4.40 ± 0.74	3.83 ± 0.30 ± 0.92	3.95
NGC 1550	2T	33.85 ± 0.49	11.61 ± 0.93	10.63 ± 0.27	9.38 ± 1.28	2.24 ± 0.49 ± 1.61	1.33
NGC 2563	1T	17.13 ± 0.43	7.85 ± 0.79	7.70 ± 0.22	0.75 ± 0.06	0.82 ± 0.43 ± 0.82	0.89
NGC 4325	1T	13.07 ± 0.49	6.62 ± 0.79	5.69 ± 0.21	0.71 ± 0.03	0.04 ± 0.49 ± 0.82	0.04
NGC 5044	2T	22.40 ± 0.33	8.10 ± 0.65	9.01 ± 0.19	3.33 ± 0.11	1.96 ± 0.33 ± 0.68	(2.58)
NGC 5846	2T	25.15 ± 0.59	12.59 ± 1.01	10.47 ± 0.34	0.35 ± 0.03	1.74 ± 0.59 ± 1.06	1.43
NGC 6329	1T	17.47 ± 0.49	8.09 ± 0.81	7.02 ± 0.23	1.14 ± 0.17	1.22 ± 0.49 ± 0.84	1.25
NGC 6521	1T	13.57 ± 0.44	5.90 ± 0.71	5.64 ± 0.19	1.52 ± 0.44	0.52 ± 0.44 ± 0.73	0.60
NGC 7619	1T	15.31 ± 0.37	7.46 ± 0.75	6.71 ± 0.18	0.32 ± 0.03	0.81 ± 0.37 ± 0.77	0.95
Pavo	2T	10.20 ± 0.42	5.60 ± 0.67	4.11 ± 0.15	0.51 ± 0.25	-0.02 ± 0.42 ± 0.73	-0.03
RGH 80	1T	10.94 ± 0.29	4.61 ± 0.55	4.44 ± 0.11	0.34 ± 0.05	1.55 ± 0.29 ± 0.56	2.45
S49-147	2T	23.96 ± 0.61	11.26 ± 0.90	10.53 ± 0.36	0.57 ± 0.19	1.59 ± 0.61 ± 0.99	1.37

* IGM model ID. "1T" means vMEKAL and "2T" means 2-vMEKAL models.

[†] Rates in 10^{-3} cts s^{-1} GIS $^{-1}$. Errors are statistical 1σ .

[‡] Rates in 10^{-3} cts s^{-1} GIS $^{-1}$. Errors are from fluctuation, 1σ .

[§] Rates in 10^{-3} cts s^{-1} GIS $^{-1}$. Errors are systematic, 1σ .

^{||} Rates in 10^{-3} cts s^{-1} GIS $^{-1}$. See text for the IGM error.

[#] Statistical 1σ and quadrature sum of all systematic 1σ errors.

** Significance of excess rates compared to the quadrature sum of all 1σ errors. Value of NGC 5044 is presented with brackets, because the IGM model fit in the soft band is not acceptable even at 99% confidence.

Table 6. Results from fitting to the full band spectra with a model with and without a power-law.

target	Model*	kT_1 [†] (keV)	kT_2 [‡] (keV)	Abundance $Z_{Fe}(Z_{\odot})$	F_{hard} [§]	$F_{soft}^{IGM }$	χ^2/dof	$\Delta\chi^2$ [#]
HCG 62	2T/2Z	0.94 ^{+0.04} _{-0.04}	17.5 ^{+∞} _{-11.8}	0.17 ^{+0.04} _{-0.01}	-	4.7	84.4/66	-
	2T/2Z+PL	0.71 ^{+0.12} _{-0.08}	1.20 ^{+0.33} _{-0.14}	0.30 ^{+0.15} _{-0.07}	1.34 ^{+0.25} _{-0.26} ± 0.53	4.4	61.3/64	23.1
NGC 1399	2T/6Z	0.88 ^{+0.19} _{-0.03}	1.79 ^{+0.21} _{-0.09}	0.78 ^{+0.08} _{-0.15}	-	17.3	224.8/173	-
	2T/6Z+PL	0.84 ^{+0.04} _{-0.06}	1.58 ^{+0.11} _{-0.13}	0.63 ^{+0.12} _{-0.11}	1.90 ^{+0.64} _{-0.61} ± 0.45	16.5	195.2/171	29.6
RGH 80	1T/2Z	1.26 ^{+0.05} _{-0.05}	-	0.22 ^{+0.06} _{-0.04}	-	1.8	111.5/66	-
	1T/2Z+PL	1.08 ^{+0.03} _{-0.04}	-	0.32 ^{+0.21} _{-0.10}	0.69 ^{+0.13} _{-0.14} ± 0.37	1.3	58.2/64	53.3

* Model ID. "1T" means vMEKAL, and "2T" means 2-vMEKAL models. "2Z" means that the metal abundances are grouped into two (Z_{α} and Z_{Fe}). "6Z" means models with Mg, Al, Si and S set free, in addition to "2Z". "PL" mean the $\Gamma = 2.0$ fixed power-law component.

[†] Temperature of the cooler component.

[‡] Temperature of the hotter component, when fitted with the 2-vMEKAL model.

[§] 2-10 keV flux of the power-law component, in 10^{-12} erg s^{-1} cm $^{-2}$. The second error represents the value of 90% CXB fluctuation.

^{||} 0.7-2.5 keV flux of the IGM component. (10^{-12} erg s^{-1} cm $^{-2}$)

[#] Improvement of χ^2 by adding a power-law component (addition of 2 parameters).

4.4.1. The HCG 62 group

This is a bright group of galaxies, emitting a 0.7–2.5 keV flux of 4.7×10^{-12} erg s^{-1} cm $^{-2}$. To investigate the nature of the excess hard emission in this source, we analyzed the full band spectra. The GIS spectra were fitted over the 1–8 keV range, while those of the SIS were used up to 4.5 keV determined from the source brightness and background uncertainty.

The 2-vMEKAL model provided unacceptable fit to the full band data with $\chi^2/dof = 84.4/66$. By adding a power-law component with a photon index Γ fixed at 2.0 (2-vMEKAL+PL model), an acceptable fit was obtained

with $\chi^2/dof = 61.3/64$. According to an F -test, the probability of this improvement being by chance is less than 10^{-4} . The results of both fits are presented in table 6, and the fit with the latter model is presented in figure 8. The power-law flux in the 2–10 keV band, F_{hard} , amounts to $\sim 30\%$ of the IGM component flux in the 0.7–2.5 keV band, F_{soft}^{IGM} . These results generally agree with Fukazawa et al. (2001). The excess above the 2-vMEKAL fit can also be reproduced by a bremsstrahlung model instead of the power-law, although the bremsstrahlung temperature becomes rather high as $4.0_{-1.3}^{+8.3}$ keV. Thus, the data clearly requires a non-thermal, or less likely, very hot thermal

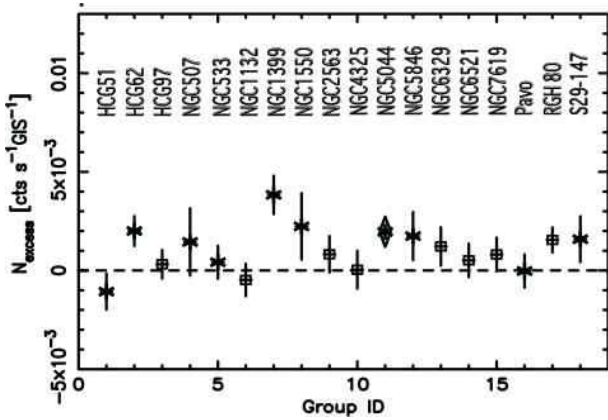


Fig. 7. Significance of the excess count rate in the GIS 4–8 keV spectra, above the IGM model determined in the energy range below 2.5 keV. Open boxes show those objects of which the soft-band data are reproduced with the vMEKAL model, while stars those which require 2-vMEKAL modeling. Error bars refer to the quadrature sum of statistical and systematic 1-sigma uncertainties. Result of NGC 5044, in which the soft-band fit is not acceptable in 99% confidence, is shown with a diamond.

component. If Γ is set free in the above 2-vMEKAL+PL fit, we obtain $\Gamma = 2.17^{+0.28}_{-0.53}$ with $\chi^2/\text{dof} = 60.8/63$, implying that the improvement is insignificant. For reference, the 90% fluctuation level of the CXB brightness is separately presented in the error column of F_{hard} in table 6. Again, the CXB fluctuation is insufficient to explain the hard excess, confirming the results presented in section 4.3.

Figure 9 shows the azimuthally-averaged radial profile of the 4.0–8.0 keV GIS count rate from HCG 62, compared with the background profile obtained as described in section 3. Regions around the five point sources in the HCG 62 field are excluded. Thus, the comparison reconfirms the highly significant hard X-ray signal, of which only $\sim 25\%$ can be accounted for by the thermal IGM emission as revealed by figure 8. The emission is clearly extended and detectable up to $\sim 15'$, beyond which it vanishes in agreement with the background scaling correction employed in section 3.

To further examine the consistency between the spectral (figure 8) and spatial (figure 9) results, we sorted the spectra into three concentric annuli, and performed the 2-vMEKAL+PL fit to each. As described in table 7, the power-law component is required in all annuli. The central $3'$ of the group is well fitted with a vMEKAL+PL model, but 2-vMEKAL+PL fit provides significantly improved results in view of an F -test. The outer regions can be fitted with a single vMEKAL model on condition that the $\Gamma = 2.0$ power-law is added. Therefore, the extended nature of the excess hard X-ray emission, indicated by figure 9, is supported by the spectral analysis as well.

Buote (2000) analyzed the same ASCA data accumulated from the central $\sim 3'$ region, and fitted the spectra with a combination of 0.7 keV and 1.4 keV thermal components with ~ 1 solar metal abundances. While the

reported temperatures agree with our measurements, he did not mention the excess hard component in his paper, possibly because he used the energy range below ~ 5 keV. This limited energy range, in turn, was required presumably by a more conventional background subtraction method employed. Actually, we can reproduce his results if we ignore the energy range above 4 keV and set the absorption column free, as he did.

Recently, Morita et al. (2006) analyzed the XMM-Newton and Chandra data of HCG 62, and obtained a radial temperature profile which is 0.7–0.8 keV within $1'$ and is increasing to 1.4 keV at $2' - 4'$. Again, the measured temperatures are consistent with our 2-vMEKAL+PL results from the $r < 3'$ spectra. They did not detect the excess hard X-rays in their data. Instead, they included the emission by scaling the parameters of Fukazawa et al. (2000) as a background in their analysis. They argue that their results did not significantly change with and without this component. Non detection by Chandra and XMM is not surprising, since their 4–8 keV background count rate, normalized to the effective area and the sky area, is 8 and 4 times higher than that of the GIS, respectively (figure 1). Specifically, the hard excess emission from HCG 62 amounts to 12% of the 4–8 keV GIS background (CXB+NXB), whereas it is only $\sim 3\%$ of the total background of XMM; this is smaller than the background modeling uncertainty of $\sim 5\%$, obtained after sophisticated screening (e.g. Nevalainen et al. 2005).

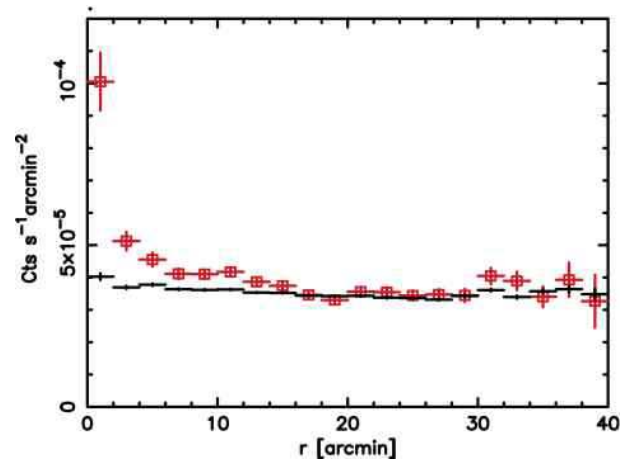


Fig. 9. The 4.0–8.0 keV GIS radial count-rate profile, shown as a function of two-dimensional radius from the group center. The on-source data are shown in red, and the background in black. Abscissa is in arcmin, while ordinate is in $\text{cts s}^{-1} \text{arcmin}^{-2}$.

4.4.2. The NGC 1399 group

Since the NGC 1399 group (the Fornax cluster) is one of the X-ray brightest groups in the sky, the data have very high statistics, requiring careful analyses. The soft-band spectra can be approximated by two temperatures of 0.8 keV and 1.4 keV (table 4), which are consistent with the virial temperature of ~ 1 keV implied by the galaxy velocity dispersion of 374 km s^{-1} (Drinkwater et al. 2001).

Table 7. Fit results to the radially sorted SIS+GIS spectra of HCG 62, with the model including power-law.

Region	kT_1 * (keV)	kT_2 † (keV)	Abundance		F_{hard} ‡	$F_{\text{soft}}^{\text{IGM}}$ §	χ^2/dof	$\Delta\chi^2$
			Z_α	Z_{Fe}				
$0' < r < 3'$	$0.87^{+0.03}_{-0.01}$	-	$0.69^{+0.25}_{-0.24}$	$0.34^{+0.19}_{-0.10}$	$0.26^{+0.04}_{-0.04}$	1.11	77.3/66	79.3
	$0.77^{+0.05}_{-0.14}$	$1.42^{+0.27}_{-0.34}$	$1.26^{+2.43}_{-0.63}$	$0.69^{+1.11}_{-0.27}$	$0.25^{+0.07}_{-0.04}$	1.24	55.8/63	23.9
$3' < r < 7'.5$	$1.10^{+0.18}_{-0.05}$	-	$0.26^{+0.13}_{-0.11}$	$0.16^{+0.14}_{-0.08}$	$0.30^{+0.08}_{-0.08}$	1.06	58.6/64	33.2
$7'.5 < r < 15'$	$0.84^{+0.16}_{-0.09}$	-	$0.13^{+0.26}_{-0.13}$	$0.15^{+0.11}_{-0.06}$	$0.66^{+0.14}_{-0.16}$	1.72	59.8/58	37.6
$3' < r < 15'$	$0.97^{+0.06}_{-0.09}$	-	$0.19^{+0.15}_{-0.11}$	$0.17^{+0.06}_{-0.04}$	$0.92^{+0.18}_{-0.17}$	2.71	73.2/65	67.8

* Temperature of the IGM model. In 2-vMEKAL models, a cooler component value is presented.

† Temperature of the hotter component in 2-vMEKAL models.

‡ The 2-10 keV flux of the power-law emission. (10^{-12} erg s $^{-1}$ cm $^{-2}$)

§ The 0.7-2.5 keV flux of the IGM emission. (10^{-12} erg s $^{-1}$ cm $^{-2}$)

|| Improvement of χ^2 by adding a power-law component (addition of 2 parameters). In all cases, the improvement were significant by (1/1000) by F-test.

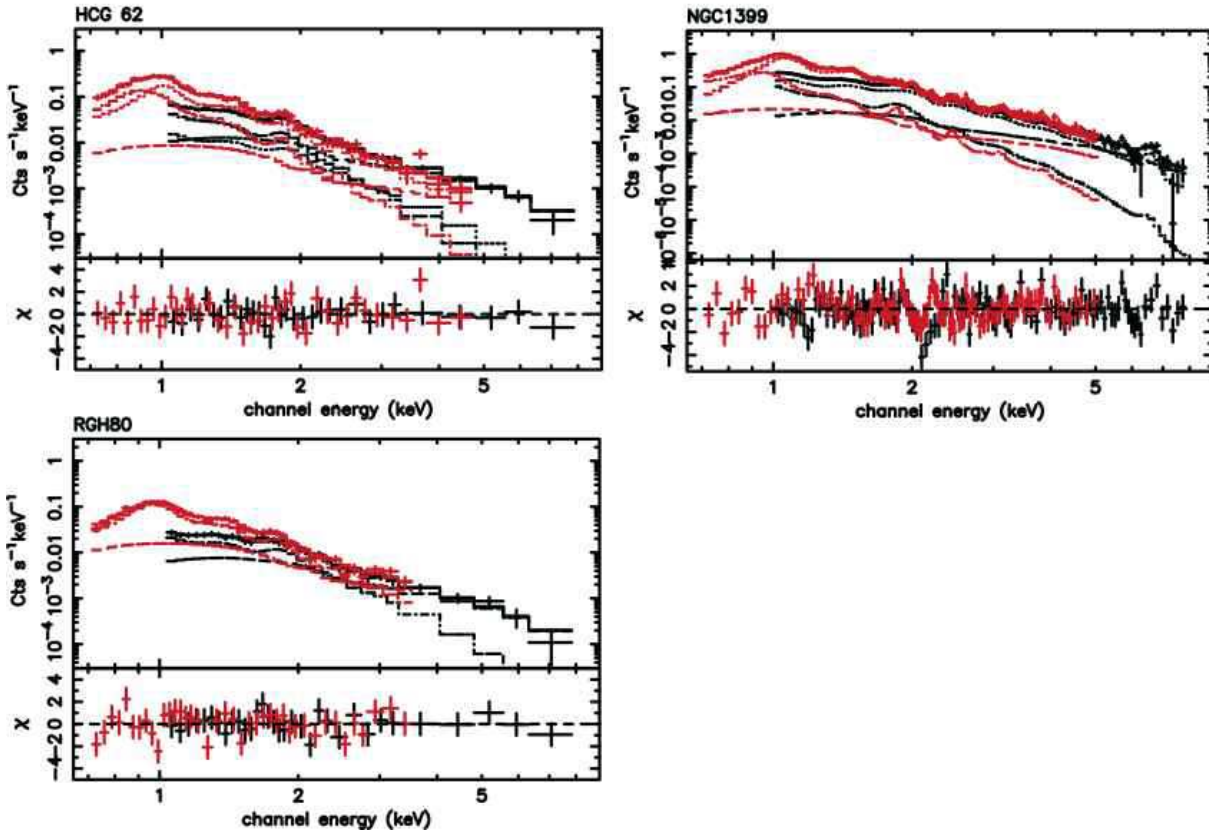


Fig. 8. Results of the joint 2-vMEKAL+PL model fitting to the GIS and SIS spectra of HCG 62 and NGC 1399. Those of RGH 80 fitted with vMEKAL+PL model is also presented. See text for detail.

Compared to these, the hard-band derived temperature, $kT_{\text{H}} = 1.84^{+0.09}_{-0.11}$ keV (table 3), is significantly higher, suggesting the presence of a harder emission component.

As an attempt to further examine the issue, we started with fitting the 2-vMEKAL model to the full band spectra. The abundances of Mg, Al, Si, and S were set free in addition to Z_α and Z_{Fe} . The fit was far from acceptable (with $\chi^2/\text{dof} = 292.1/191$), due to the possible calibration discrepancies around 1.2 and 2.1 keV mentioned in section 4.2.4. By ignoring the energy bands of 1.15–1.25 keV and 2.1–2.2 keV, the 2-vMEKAL model fit

improved to $\chi^2/\text{dof} = 224.8/173$, but was still unacceptable by 99.5%. By further adding a power-law with fixed $\Gamma = 2.0$ (2-vMEKAL+PL model), we have finally obtained an acceptable fit by 90% level (with $\chi^2/\text{dof} = 195.2/171$). The results are presented in table 6 and figure 8. (In the figure, the two ignored energy bands are restored for clarity.) The power-law flux F_{hard} is 12% of $F_{\text{soft}}^{\text{IGM}}$.

In the 2-vMEKAL fit after ignoring the two energy bands, the best fit value of the hotter component temperature is derived as $kT_2 = 1.79$ keV. Since it is close to $kT_{\text{H}} = 1.84$, and since the 2-vMEKAL fit is almost suc-

cessful, a careful examination is needed to judge if the data is really requiring the hard component. The improvement by adding a power-law component is $\Delta\chi^2 = -29.6$, which is significant with the chance probability of less than 10^{-5} in terms of an F -test. Furthermore, the resultant fit with 2-vMEKAL+PL model is statistically acceptable. Therefore, the excess hard X-ray emission is likely to be present in the NGC 1399 group as well. If we replace the power-law with a third thermal component, a similarly good ($\chi^2/\text{dof}=189.6/170$) full-band fit can be obtained. In this case, however, the temperature become as high as $3.2_{-0.9}^{+2.6}$ keV. Thus, the excess hard component in this object can be explained by a $\Gamma = 2.0$ power-law emission which is possibly of non-thermal nature, or a very hot thermal emission with a temperature of $\gtrsim 3$ keV.

4.4.3. The RGH 80 group

The last of the 3 selected objects, RGH 80 is the most distant one in our sample, yet showing rather strong hard X-ray signals above the extrapolated IGM contribution. The full band fit with a single vMEKAL model was not acceptable (with $\chi^2/\text{dof} = 111.5/66$). When we added a power-law component with Γ again fixed at 2.0, the fit greatly improved and became acceptable with $\chi^2/\text{dof} = 58.2/64$ (see table 6 and figure 8). Although the absolute value of F_{hard} itself is rather low, it amounts to $\sim 50\%$ of $F_{\text{soft}}^{\text{IGM}}$. When we added a second thermal component in place of the power-law (2-vMEKAL model), a similarly good fit was obtained with $\chi^2/\text{dof} = 58.7/63$. However, the obtained hotter temperature is $kT_2 = 11.0_{-8.3}^{+\infty}$ keV, that is, higher than 2.7 keV. Since this value is considerably higher than the cooler one ($kT_1 = 1.09_{-0.04}^{+0.07}$ keV) and much exceeding typical virial temperatures of galaxy groups, the excess hard signals are likely to be of non-thermal origin. These properties make this object resemble HCG 62, but with poorer statistics.

Boute (2000) analyzed the ASCA spectra of RGH 80 derived from the central $\sim 3'.6$, using also a two temperature thermal emission model, to obtain a hotter temperature of $kT_2 = 1.64_{-0.17}^{+0.21}$ keV. Although this is apparently inconsistent with our results, we confirmed that we can reproduce the Boute's result by extracting the spectra from a similar region. Therefore, the hard emission is inferred to be stronger in the $3' < r < 10'$ region.

5. Discussion

5.1. Summary of analysis results

Through ASCA observations of 18 near-by low temperature galaxy groups, indication of excess hard component was obtained from 3 objects. The excess first manifested itself as large differences between the temperatures inferred in the soft band below 2.5 keV (kT_{S}) and in the hard band above 2.5 keV (kT_{H}), which are determined mainly by the Fe-L emission lines and the bremsstrahlung continuum, respectively.

In order to quantify the suggested hard-band excess, we represented the IGM emission by vMEKAL or 2-vMEKAL model determined in the energy range below 2.5 keV, and extrapolated it to the 4–8 keV GIS range.

Then, even taking fully into account the CXB fluctuation and the NXB estimation error, three objects (HCG 62, NGC 1399, and RGH 80) showed significant ($> 2\sigma$) excess counts above the expected IGM contribution (section 4.3). From the full band fitting to these objects (section 4.4), we found that the excess can be successfully represented by a $\Gamma = 2.0$ power-law model, and hence it is likely to be of non-thermal origin, particularly in HCG 62 and RGH 80. The spectra of NGC 1399 can be explained either by adding a non-thermal emission with a flux of about 10% of that of the IGM, or the third thermal component having a temperature $\gtrsim 3$ keV.

5.2. Hard X-ray excess compared to other parameters

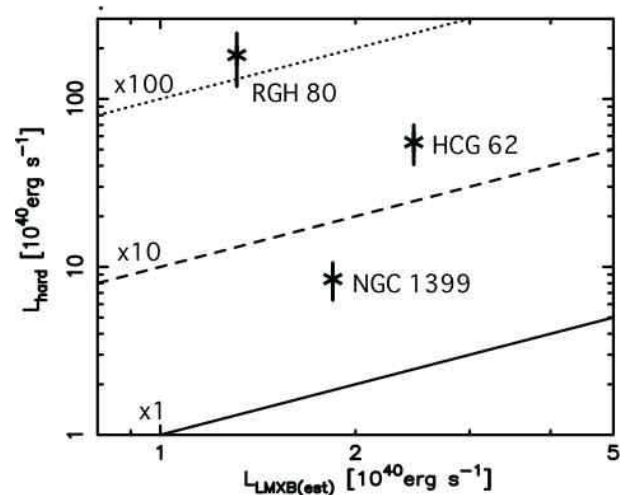


Fig. 10. Excess hard luminosity, L_{hard} , compared with L_{LMXB} which is derived from the X-ray to optical flux ratios of elliptical galaxies. Solid, dashed and dotted lines represent, 1, 10 and 100 times of L_{LMXB} , respectively.

In section 4.4, we derived the value of F_{hard} and the associated errors for HCG 62, NGC 1399 and RGH 80. In this section, we briefly compare it to other parameters of these objects. The calculated 2–10 keV luminosity of the power-law component, L_{hard} , is presented in table 8, together with the 0.7–2.5 keV luminosity of the IGM component ($L_{\text{soft}}^{\text{IGM}}$). Both the values of F_{soft} and kT_{S} of the three objects are typical in our sample. In addition, some other objects in our sample have similar temperatures and IGM luminosities to the three object, yet without excess hard signals. The lack of correlations to these parameters suggests that the phenomenon we have been studying is not likely to be artifacts caused by wrong background subtraction, or incorrect modeling of the IGM contribution.

An elliptical galaxy is known to emit an X-ray component with a rather hard spectrum, as a sum of discrete sources in it, such as LMXBs in particular (Canizares et al. 1987; Matsushita et al. 1994; Matsushita et al. 2000). This component could provide a possible explanation to the hard excess emission, because LMXB spectra, approximated by a thermal bremsstrahlung with $kT \sim 10$ keV, are generally consistent with what has been observed in

Table 8. Luminosity of the IGM and excess emission of HCG 62, NGC 1399 and RGH 80. Estimated contribution from LMXBs in the member galaxy is also shown.

target	$L_{\text{soft}}^{\text{IGM}}$ *	L_{hard} †	L_{LMXB} ‡
HCG 62	181.2	55.3 ± 14.6	2.5
NGC 1399	73.7	8.5 ± 2.1	1.8
RGH 80	341.1	182.4 ± 63.7	1.3

* Luminosity of the IGM emission in 0.7-2.5 keV, in unit of 10^{40} erg s $^{-1}$.

† Luminosity of the excess hard emission in 2-10 keV, in unit of 10^{40} erg s $^{-1}$. Errors are 1σ including both the statistical and systematic origins.

‡ Luminosity of the expected LMXB emission in 0.7-2.5 keV, in unit of 10^{40} erg s $^{-1}$.

the present study. The integrated 2–10 keV discrete-source luminosity, L_{LMXB} , of each elliptical galaxy is known to be approximately proportional to its B-band luminosity, L_B . We hence estimated L_{LMXB} in our sample objects, using L_B given in table 1 and the relation of $L_{\text{LMXB}} = 4 \times 10^{39} (L_B / 10^{10} L_{\odot})$ erg s $^{-1}$ (converted from Matsushita et al. 2000). The result, presented in figure 10, shows that L_{hard} of HCG 62, NGC 1399 and RGH 80 is 20, 5 and 140 times higher than the estimated L_{LMXB} , respectively. Thus, the discrete-source contribution cannot explain away the hard-excess phenomenon. Similar excess hard X-ray fluxes from a few Virgo elliptical galaxies were reported by Loewenstein et al. (2001).

5.3. Possible Emission Mechanisms

Even in the case of HCG 62 which shows the most significant hard X-ray excess, the spectral shape of the excess emission is not well constrained; $\Gamma = 2.17_{-0.53}^{+0.28}$. Therefore, it is rather difficult to tell whether the emission is of thermal or non-thermal origin. In this section, we briefly discuss both scenarios, using HCG 62 as a representative case.

5.3.1. Non-thermal interpretation

In the non-thermal scenario, two possibilities are generally discussed: inverse Compton (IC) emission from GeV electrons as they scatter off the cosmic microwave background photons, and non-thermal bremsstrahlung from sub-relativistic particles interacting with ambient plasmas (see e.g. Sarazin 1999 and Sarazin, Kempner 2000). However, the latter is unlikely, because of too low an efficiency (e.g. Petrosian 2001); sub-relativistic electrons suffer from 4 to 5 orders of magnitude larger energy loss in their Coulomb interactions with ambient ions, than their bremsstrahlung loss, making the energetics unrealistic (e.g. Fukazawa et al. 2001). Therefore, below we consider only the IC interpretation.

In the IC scenario, the postulated GeV electrons should also emit synchrotron photons in the radio band. There is however no reported radio halo detection of HCG 62, and the 365 MHz Texas catalog (Douglas et al. 1996) gives an upper limit of ~ 0.4 Jy on the radio flux density from HCG 62. The comparison of this upper limit with our $F_{\text{hard}} \sim 1.3 \times 10^{-12}$ erg s $^{-1}$ cm $^{-2}$ in the 2-10 keV band yields an upper limit on the volume-averaged magnetic field as $B \sim 0.1$ μ G, assuming that a single population of

electrons with an energy index of 3.0 are emitting both IC and synchrotron components under a uniform magnetic field. As already mentioned in Fukazawa et al. (2001), this limit appears too low for intra-group magnetic fields. Introduction of non-uniform magnetic fields and/or time evolution of the electron energy distribution (e.g. high-energy cutoff) may solve this discrepancy. For example, Brunetti et al. (2001) proposed a model explaining the non-thermal signature of the Coma cluster. In this cluster, observed radio halo flux and the hard X-ray flux suggested by Beppo-SAX (e.g. Fusco-Femiano et al. 1999) leads to a similarly low magnetic field (~ 0.1 μ G) when a simple model for electron population is employed. By incorporating the radial dependence of magnetic field and assumed (re)-acceleration power, as well as the time evolution, in particular introducing the re-acceleration phase which modifies the electron spectra flatter with distinctive cut-off, they successfully reproduced the Coma results. Similar models may be able to explain the HCG 62 results.

When $B < 3$ μ G, the electrons are expected to lose their energies predominantly in the IC channel. Therefore, to sustain $L_{\text{hard}} \sim 4 \times 10^{41}$ erg s $^{-1}$ under a steady-state condition, a comparable energy input should be supplied to the electrons. The recent Chandra detection of a pair of ‘‘X-ray cavities’’ near the central galaxy (NGC 4761) of HCG 62 (Vrtilek 2000⁴, Morita et al. 2006) suggests a past AGN activity, which may well have supplied the needed energy input. Although NGC 4761 currently shows little evidence of AGN activity, the scenario remains intact if the putative AGN activity continued till 1 Gyr ago or later, because the cooling time of a 1 GeV electron due to the IC process is ~ 1 Gyr.

Since HCG 62 is a compact group with a high galaxy density and a rather large velocity dispersion of 376_{-46}^{+52} km s $^{-1}$ (Zabludoff, Mulchaey 1998), energy inputs may also be possible from magneto-hydrodynamic interactions of the member galaxies with the IGM (Makishima et al. 2001). Thus, the non-thermal interpretation is promising from the energetics view point.

5.3.2. Thermal interpretation

If the hard excess in our sample objects are interpreted as thermal emission, the inferred temperature ranges from ~ 3 keV or higher. In order to explain L_{hard} that amounts

⁴ <http://chandra.harvard.edu/photo/2001/hcg62/>

to up to 25% of L_{soft} , then the putative hotter gas must fill > 70% of the group volume, assuming that it is in a pressure balance with the ~ 1 keV IGM. That is, the hotter gas is implied to be energetically dominant in the intra-group space. Since the velocity dispersion of HCG 62 as quoted above translates to a virial temperature of only ~ 1 keV (e.g. Xue, Wu, 2000), the postulated gas is concluded to be significantly hotter than the gravitational potential felt by the galaxies. However, if the gas were gravitationally unbound and freely escaping with sound velocity, the necessary energy input would become enormous, because the escape time of a 2 keV gas is two orders of magnitude shorter than its radiative cooling time, assuming a representative density of $\sim 3 \times 10^{-4} \text{ cm}^{-3}$.

Another possibility is that such an object is surrounded by a much deeper gravitational potential halo with a considerably larger scale. Actually, the presence of such a large-scale halo has been suggested by Matsushita et al. (1998) around the elliptical galaxy NGC 4636. In any case, the presence of such a hot gaseous component would have a profound impact on the structure and formation of galaxy groups.

6. Conclusion and future prospect

From the detailed analysis of the hard (> 2.5 keV) band X-ray spectra of groups of galaxies obtained with ASCA, evidence of excess hard X-ray emission has been suggested from 3 out of 18 objects investigated. They are HCG 62, NGC 1399 and RGH 80. The emission cannot be explained by either fluctuations in the CXB brightness, the NXB estimation error, or contributions of point sources in the member galaxies. The excess cannot be explained away by assuming a moderate temperature gradient in the IGM, either. At least in HCG 62, the hard X-ray emission is as extended as the thermal IGM emission.

The observed excess hard X-ray emission can be modeled by a power law with photon index fixed at 2.0, or a high-temperature thermal component, although it is difficult to distinguish them. If considered to be of non-thermal origin, the observed hard X-ray emission can be most reasonably interpreted as inverse-Compton emission by GeV electrons accelerated in these systems. In contrast, thermal interpretation of the phenomenon leads to an inference that some of groups of galaxies are surrounded by a much deeper (and probably of larger-scale) gravitational halo than those felt by the member galaxies.

In order to further promote the study, we may utilize the Suzaku mission, launched into orbit on 10th July, 2005. Actually, the X-ray Imaging Spectrometer onboard the satellite has a 6 times larger effective area than the ASCA GIS at 7 keV in total, and its background, when normalized to the solid angle and effective area, is only slightly higher than that of the GIS.

The authors are greatly thankful to the anonymous referee for critical reading and providing fruitful comments on this work.

References

- Birzan, L., Rafferty, D. A., McNamara, B. R., Wise, M. W., & Nulsen, P. E. J. 2004, *ApJ*, 607, 800
- Briel, U. G., Finoguenov, A., & Henry, J. P. 2004, *A&A*, 426, 1
- Brunetti, G., Setti, G., Feretti, L., & Giovannini, G. 2001, *MNRAS*, 320, 365
- Buote, D. A. 2000, *MNRAS*, 311, 176
- Drinkwater, M. J., Gregg, M. D. & Colless, M. 2001, *ApJ*, 548, L139
- Canizares, C. R., Fabbiano, G., & Trinchieri, G. 1987, *ApJ*, 312, 503
- de Vaucouleurs, G., de Vaucouleurs, A., Corwin, H. G., Jr., Buta, R. J., Paturel, G., & Fouque, P. 1991, *Third Reference Catalogue of Bright Galaxies* (Springer-Verlag Berlin Heidelberg New York)
- Dickey, J. M. & Lockman, F. J. 1990, *ARA&A*, 28, 215
- Douglas, J. N., Bash, F. N., Bozayan, F. A., Torrence, G. W., & Wolfe, C. 1996, *AJ*, 111, 1945
- Fadda, D., Girardi, M., Giuricin, G., Mardirossian, F., & Mezzetti, M. 1996, *ApJ*, 473, 670
- Feretti, L., & Giovannini, G. 1996, in *Extragalactic radio sources*, IAUS, ed. Ron D. Ekers, C. Fanti, & L. Padrielli (Kluwer Academic Publishers), 333
- Ferguson, H. C., & Sandage, A. 1990, *ApJ*, 100, 1
- Finoguenov, A., Jones, C., Böhringer, H., & Ponman, T. J. 2002, *ApJ*, 578, 74
- Fukazawa, Y. 1997, Ph.D. thesis, University of Tokyo
- Fukazawa, Y., Nakazawa, K., Isobe, N., Makishima, K., Matsushita, K., Ohashi, T., & Kamae, T. 2001, *ApJ*, 546, L87
- Furusho, T., Yamasaki, N. Y., Ohashi, T., Shibata, R., & Ezawa, H. 2001, *ApJ*, 561, L165
- Fusco-Femiano, R., Fiume, D. D., Feretti, L., Giovannini, G., Grandi, P., Matt, G., Molendi, S. & Santangelo, A. *ApJ*, 513, L21
- Hickson, P. 1982, *ApJ*, 255, 382
- Hwang, U., Mushotzky, R. F., Burns, J. O., Fukazawa, Y., & White, R. A. 1999, *ApJ*, 516, 604
- Ishisaki, Y. 1997, Ph.D. thesis, University of Tokyo
- Kaneda, H. et al. 1995, *ApJ*, 453, L13
- Kushino, A., Ishisaki, Y., Morita, U., Yamasaki, N. Y., Ishida, M., Ohashi, T., & Ueda, Y. 2002, *PASJ*, 54, 327
- Ledlow, M. J., Loken, C., Burns, J. O., Hill, J. M., & White, R. A. 1996, *AJ*, 112, 388
- Loewenstein, M., Valinia, A. & Mushotzky, R. F. 2001, *ApJ*, 547, 722
- Makishima, K., et al. 1996, *PASJ*, 48, 171
- Makishima, K. et al. 2001, *PASJ*, 53, 401
- Markevitch, M., et al. 2003, *ApJ*, 586, L19
- Matsushita, K. et al. 1994, *ApJ*, 436, 41
- Matsushita, K., Makishima, K., Rokutanda, E., Yamasaki, N. Y., & Ohashi, T. 1997, *ApJ*, 488, L125
- Matsushita, K. 1997, Ph. D. thesis, University of Tokyo
- Matsushita, K., Makishima, K., Ikebe, Y., Rokutanda, E., Yamasaki, N. Y. & Ohashi, T. 1998 *ApJ*, 499, L13
- Matsushita, K., Ohashi, T., & Makishima, K. 2000, *PASJ*, 52, 685
- Morita, U., Ishisaki, Y., Yamasaki, N. Y., Ota, N., Kawano, N., Fukazawa, Y., & Ohashi, T. 2006, *PASJ*, 58, 719
- Mulchaey, J. S., Davis, D. S., Mushotzky, R. F., & Burstein, D. 1996, *ApJ*, 456, 80

- Mulchaey, J. S., Davis, D. S., Mushotzky, R. F., & Burstein, D. 2003, *ApJS*, 145, 39
- Nevalainen, J., Markevitch, M., & Lumb, D. 2005, *ApJ*, 629, 172
- Ohashi, T. et al. 1996, *PASJ*, 48, 157
- Petrosian, V. 2001, *ApJ*, 557, 560
- Ramella, M., Geller, M. J., Huchra, J. P., & Thorstensen, J. R. 1995, *AJ*, 109, 1458
- Sarazin, C. L. 1999, *ApJ*, 520, 529
- Sarazin, C. L., & Kempner, J. C. 2000, *ApJ*, 533, 73
- Shafer, R. A., & Fabian, A. C. 1983, in *Early evolution of the universe and its present structure*, IAUS, (Dordrecht and Boston, D. Reidel Publishing Co.), 333
- Tanaka, Y., Inoue, H., & Holt, S. S. 1994, *PASJ*, 46, L37
- Wegner, G., Haynes, M. P., & Giovanelli, R. 1993, *AJ*, 105, 1251
- Zabludoff, A. I., & Mulchaey, J. S. 1998, *ApJ*, 496, 39